Hydrogen Bistability as the Origin of Photo-Bias-Thermal Instabilities in Amorphous Oxide Semiconductors

Youngho Kang, Byung Du Ahn, Ji Hun Song, Yeon Gon Mo, Ho-Hyun Nahm,* Seungwu Han, and Jae Kyeong Jeong*

Zinc-based metal oxide semiconductors have attracted attention as an alternative to current silicon-based semiconductors for applications in transparent and flexible electronics. Despite this, metal oxide transistors require significant improvements in performance and electrical reliability before they can be applied widely in optoelectronics. Amorphous indium–zinc–tin oxide (a-IZTO) has been considered an alternative channel layer to a prototypical indium–gallium–zinc oxide (IGZO) with the aim of achieving a high mobility (>40 cm^2 Vs^{-1}) transistors. The effects of the gate bias and light stress on the resulting a-IZTO field-effect transistors are examined in detail. Hydrogen impurities in the a-IZTO semiconductor are found to play a direct role in determining the photo-bias stability of the resulting transistors. The Al$_2$O$_3$-inserted IZTO thin-film transistors (TFTs) are hydrogen-poor, and consequently show better resistance to the external-bias-thermal stress and photo-bias-thermal stress than the hydrogen-rich control IZTO TFTs. First-principles calculations show that even in the amorphous phase, hydrogen impurities including interstitial H and substitutional H can be bistable centers with an electronic deep-to-shallow transition through large lattice relaxation. The negative threshold voltage shift of the a-IZTO transistors under a negative-bias-thermal stress and negative-bias-illumination stress condition is attributed to the transition from the acceptor-like deep interstitial H$_i^-$ (or substitutional H-DX$^-$) to the shallow H$_i^+$ (or H$_O^+$) with a high (low) activation energy barrier. Conclusively, the delicate controllability of hydrogen is a key factor to achieve the high performance and stability of the metal oxide transistors.

1. Introduction

The lack of transparency and high temperature processing in silicon-based electronics prevent their applications in transparent and flexible electronic devices.[1,2] For this purpose, semiconducting oxides have been studied intensively for use in transparent and flexible electronics, such as pixel drivers for flat panel displays (FPDs), electronic paper, skin sensor, and smart identification cards.[3–7] These emerging applications are enabled by the intriguing properties of semiconducting oxide thin-film transistors (TFTs), such as high mobility (>10 cm^2 Vs^{-1}), steep sub-threshold slope (<300 mV decade^{-1}), good transparency ($>80\%$ to visible light), and low temperature processing.[8,9] Historically, indium-based oxide materials have been used mainly as passive transparent conducting oxide (TCO) films for flat-screen displays, energy-efficient windows, light-emitting diodes, and photovoltaic cell. The controllability of the chemical compositions in the multicomponent metal oxide system enables tailoring of the electrical, optical, chemical, and physical properties. In particular, the discovery of carrier suppressors, such as Ga, Hf, Zr, etc., in multicomponent metal oxide materials allows an extension of the electronic applications from the traditional passive electrode components to the semiconducting active components for the field-effect transistors.[1,10,11] Despite these promising properties, the instability of semiconducting oxide-based TFTs under the electrical and light stress is critical hurdles against commercialization of the devices.[12]

Y. Kang, S. Han
Department of Materials Science and Engineering
and Research Institute of Advanced Materials
Seoul National University
Seoul 151-742, South Korea

B. D. Ahn, Y. G. Mo
Research and Development Center
Samsung Display
Yongin 446-711, South Korea

J. H. Song, J. K. Jeong
Department of Materials Science and Engineering
Inha University
Incheon 402-751, South Korea
E-mail: jkjeong@inha.ac.kr

H.-H. Nahm
Center for Correlated Electron Systems
Institute for Basic Science (IBS)
Seoul 151-747, South Korea
E-mail: hohyunnahm@snu.ac.kr

H.-H. Nahm
Department of Physics and Astronomy
Seoul National University
Seoul 151-747, South Korea

FULL PAPER

Intrinsic defects, such as oxygen vacancies (V_O), cation interstitials and oxygen interstitials (O_i), were suggested as the origin of this instability.[13–21] Nevertheless, the deeper insight into complex defect physics in semiconducting oxides is essential for gaining a complete understanding of the bias- and photo-instability of metal oxide-based TFTs, which is a prerequisite for developing stable materials with better performance.

In a microscopic viewpoint, the shallow donors in semiconducting oxide materials created by the photo-bias stress do not recover instantaneously to their original state, leading to a displacement retained for a prolong time of the threshold voltage in the semiconducting oxide TFTs. The microscopic mechanisms proposed to date are based on bistable centers allowing for an electronic deep-to-shallow transition, such as DX in $Al_xGa_{1-x}As$,[22] V_O in crystal ZnO (c-ZnO)/a-InGaZnO$_4$,[23–25] peroxide (O_2^{2-}),[26] and O_i[20,21] in a-InGaZnO$_4$. In particular, the photostress creates electron–hole pairs first. If the holes are captured by deep centers, such as V_O^0, $O^{2-}+ O^{2-}$ (disorder defect), and O_i^{2-} (bonded to cations), the deep centers can transform to shallow ones, such as V_O^{2+}, O_2^{2-}, and O_i^0 (attached to an anion). The recombination of these ionized defects and electrons occurs with certain activation energies, extending the lifetime of electrons in the conduction band, which leads to a negative shift in the threshold voltage (V_{TH}). Therefore, it is essential to identify the types of bistable centers in the semiconducting oxides.

Hydrogen is introduced easily in oxides as a ubiquitous impurity, and critically affects the electrical and optical properties of the host material. Many theoretical and experimental studies suggest that hydrogen impurity is responsible for the n-type conductivity of oxides.[27–30] This is because hydrogen becomes a shallow donor in two forms; interstitial H (H_i) and substitutional H at the O site (H_O) (as in c-ZnO).[27–29] Some studies reported that hydrogen annealing suppresses the instability of amorphous indium–zinc–tin oxide (a-IGZO)[31] because H passivates the instability sources, such as V_O in the form of H_O.[32] On the other hand, the present study found that the TFT instability is strongly proportional to the H-contamination profile in a-IZTO. Therefore, the H-induced instabilities of amorphous oxides are still unresolved. H-related instabilities may have two origins: (i) hydrogen impurities increase the concentrations of the presently-identified bistable centers or (ii) hydrogen impurities become bistable centers themselves. For an indirect scenario, it can be simply understood because the relative formation enthalpies of deep V_O^0 (O_i^{2-}) in O-deficient (O-rich) conditions are lower with respect to shallow V_O^{2+} (O_i^0) at the rising Fermi level (E_F), which is driven by the shallow H. On the other hand, considering the variety of the coupling between H and other defects, it is unclear if the validity of deep V_O^0 and O_i^{2-} in terms of a point defect is sustained (for example, the H-passivated V_O model in ref. [32]. Therefore, other aspects on hydrogen should be considered. Indeed, there is considerable evidence suggesting that hydrogen would be a bistable center. Recently, it was suggested that theoretically there can be acceptor-like hydrogen states with deep levels, i.e., metastable H_i^- (bonded to Zn atoms)[33] for H_i and stable H-DX$^-$ (regarded as a complex defect of $V_O^0+H_i^-$)[34] for H_O in c-ZnO. Furthermore, the concentration of n-type free carriers was measured experimentally to be much lower than the H-concentration in amorphous oxides, such as a-InGaZnO$_4$.[35] Despite this uncertainty for hydrogen, to the best of the authors' knowledge, there are no reports of the bistability of hydrogen in the amorphous phase; hence, the bistability issue remains to be examined.

On the other hand, indium–gallium–zinc oxide (IGZO) is the most popular channel material for semiconducting oxide TFTs, where the indium and gallium cations act the mobility enhancer and carrier suppressor, respectively.[1,4,9] Although increasing the indium fraction in IGZO allows an enhanced charge carrier mobility from the low electron effective mass and efficient intercalation of the In 5s orbital in In$_2$O$_3$, the electrical and optical stabilities of the resulting device deteriorate due to the easier creation of V_O in an indium-rich composition.[36,37] The mobility of IGZO TFTs with an acceptable stability is limited to ≈10 cm^2 Vs^{-1}. To meet the requirements of the high resolution (>200 pixels per inch), large area (>60 in.), high frame rate (>240 Hz), and 3D visual effects for the next generation FPDs, flexible and/or transparent display, the field-effect mobility need to be improved to more than 30 cm^2 Vs^{-1}.[4]

In this study, the a-IZTO film was chosen as the channel layer for the semiconducting oxide TFTs because a substantially higher field-effect mobility can be obtained because of the synergic intercalation of the 5s orbital of indium and tin atoms.[38] To examine the effects of hydrogen contamination on the light- and bias-induced instabilities of a-IZTO, two types of a-IZTO TFTs with a different hydrogen content in the channel layer were fabricated. The a-IZTO TFTs with a hydrogen-rich channel (hereafter referred as a control device) exhibited a promising high saturation mobility (μ_{SAT}) of 48.0 cm^2 Vs^{-1}, low subthreshold gate swing of 0.14 V decade^{-1}, threshold voltage of 0.4 V and $I_{ON/OFF}$ ratio of 10^9. In contrast, the μ_{SAT} value was reduced to 20.5 cm^2 Vs^{-1} for hydrogen-poor a-IZTO TFTs, whereas the other device parameters were comparable to those of the control device. On the other hand, the positive (PBTS), negative-bias-thermal stress (NBTS) and negative-bias-illumination stress (NBIS) stabilities for the hydrogen-poor a-IZTO TFTs were much better than those of the control device. We also examined the hydrogen-related electronic states in a-IZTO semiconductors thoroughly using first-principles calculations. The electronic structure calculation indicated that the bistable hydrogen impurities are generally responsible for the V_{TH} instabilities under various bias and photo-bias stress conditions in metal oxide semiconductors. To date, ubiquitous hydrogen impurity has been considered an assistant that can alter the electronic properties and concentration of deep trap centers, such as oxygen vacancies, oxygen interstitials, and peroxide in the host material. These results can provide a comprehensive single framework to understand the PBTS, NBTS, and NBIS instability of any semiconducting oxide TFT based on the simultaneous consideration of well-known deep trap centers and hydrogen impurities.

2. Results and Discussion

2.1. Performance and Photo-Bias-Thermal-Stress instabilities of a-IZTO TFTs

Two a-IZTO TFT devices were fabricated, in which the hydrogen concentration was tuned differently to examine the
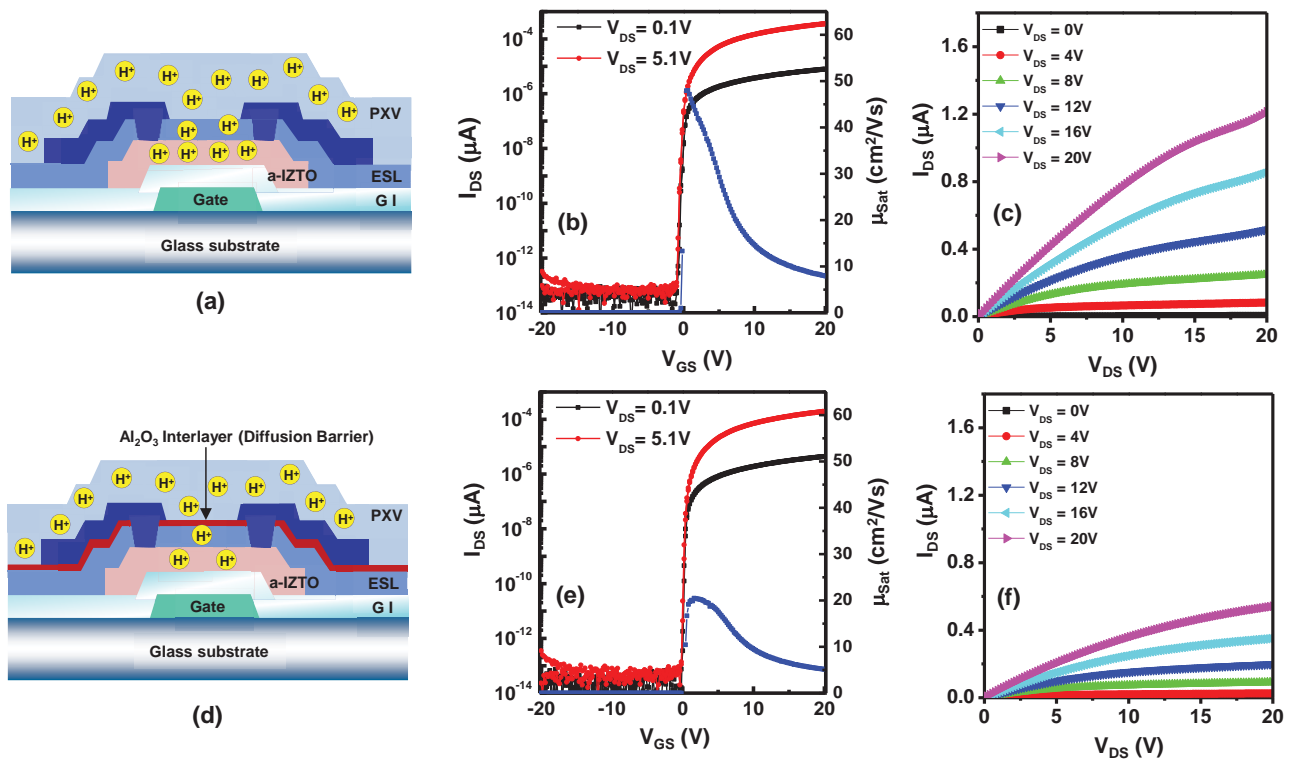
www.MaterialsViews.com

ADVANCED
ELECTRONIC
MATERIALS
www.advelectronicmat.de

FULL PAPER

Figure 1. Schematic cross-section of the a) control and d) Al$_2$O$_3$-inserted a-IZTO TFTs. Representative transfer characteristics for the b) control and e) Al$_2$O$_3$-inserted a-IZTO TFTs: the corresponding output characteristics for the c) control and f) Al$_2$O$_3$-inserted a-IZTO TFTs.

effect of hydrogen impurities on the mobility and instability of the a-IZTO field-effect transistors. **Figure 1**a,d shows a schematic cross-section of the a-IZTO TFTs without (control device) and with an Al$_2$O$_3$ interlayer (referred to as Al$_2$O$_3$-inserted device), respectively. The PECVD-derived SiO$_2$ passivation layer contained a huge hydrogen concentration, which was controlled by feeding a high flow rate of SiH$_4$ gas to the reactor during the deposition process. In the case of the control device, the hydrogen in the passivation SiO$_2$ layer would diffuse into the a-IZTO channel layer through the underlying etch stop layer (ESL) SiO$_2$ film during post deposition annealing (PDA) at 350 °C (Figure 1a). In contrast, the Al$_2$O$_3$-inserted device would have a lower hydrogen concentration in the a-IZTO channel layer because rf-sputtered Al$_2$O$_3$ films have excellent diffusion barrier properties against hydrogen permeation (Figure 1d). Figure 1b,e shows the representative transfer characteristics of the control and Al$_2$O$_3$-inserted a-IZTO TFTs. The field-effect mobility (μ_{SAT}) was determined from the maximum incremental slope of an $I_{DS}^{1/2}$ versus V_{GS} plot in the saturation region according to the following equation: $I_{DS} = (WC_i/2L)$ $\mu_{SAT}(V_{GS}-V_{TH})^2$, where L is the channel length, W is the width,

and C_i is the gate capacitance per unit area. The V_{TH} was determined from the gate voltage (V_{GS}) needed to produce a drain current of $L/W \times 10$ nA at $V_{DS} = 5.1$ V. The subthreshold gate swing (SS = dV_{GS}/dlogI_{DS}) was extracted from the linear portion of a plot of the log I_{DS} versus V_{GS}. The a-IZTO TFTs without an Al$_2$O$_3$ interlayer (control device) exhibited a high μ_{SAT} of 48.0 cm^2 Vs^{-1}, low SS of 0.15 V decade^{-1}, V_{TH} of 0.4 V, and $I_{ON/OFF}$ ratio of 10^{10}. The high mobility for the a-IZTO TFTs was achieved without compromising the $I_{ON/OFF}$ ratio because the $I_{ON/OFF}$ ratio ($\geq 10^8$) and field-effect mobility are equally important in designing a practical active-matrix pixel backplane. Although a high mobility exceeding 60 cm^2 Vs^{-1} for the oxide TFTs has been reported frequently, they suffer from a low $I_{ON/OFF}$ ratio presumably due to the high conductivity of the channel layer, ill-defined channel dimensions or inadequately high gate leakage current.[39–41] On the other hand, the μ_{SAT} and V_{TH} values for the a-IZTO TFTs with an Al$_2$O$_3$ interlayer were reduced to 20.5 cm^2 Vs^{-1} and positively displaced to 1.4 V, respectively (Figure 1e), whereas the $I_{ON/OFF}$ ratio was comparable to the control device, as summarized in **Table 1**. The corresponding output characteristics for the control and

Table 1. Device parameters including μ_{SAT}, SS, V_{th}, $I_{on/off}$, $D_{it, max}$, and $N_{ss, max}$ of the control and Al$_2$O$_3$-inserted a-IZTO TFTs.

Sample	μ_{SAT} [cm^2 Vs^{-1}]	SS [V decade^{-1}]	V_{th} [V]	$I_{on/off}$	$D_{it, max}$ [eV^{-1} cm^{-2}]	$N_{ss, max}$ [eV^{-1} cm^{-3}]
Control device	48.0	0.15	0.4	10^{10}	2.3×10^{11}	4.6×10^{16}
Al$_2$O$_3$-inserted device	20.5	0.10	1.4	10^{10}	1.6×10^{11}	3.1×10^{16}

ADVANCED
ELECTRONIC
MATERIALS
www.advelectronicmat.de
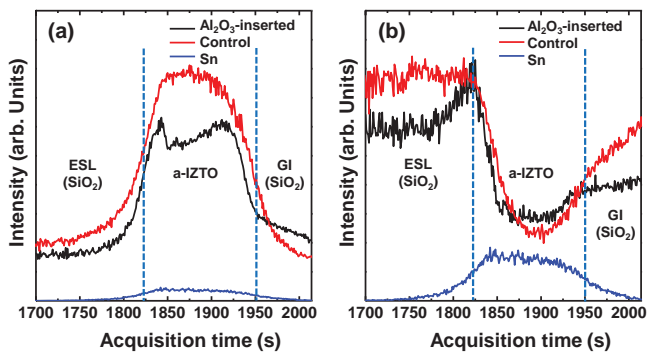
Materials
Views
www.MaterialsViews.com

Figure 2. SIMS depth profile of a) OH⁻ and b) hydrogen concentration in a-IZTO thin films for the control and Al_2O_3-inserted devices.

Al_2O_3-inserted a-IZTO TFTs were shown in Figure 1c,f. The output current of the Al_2O_3-inserted device was diminished due to its lower mobility compared to the control device.

To explain the different mobility of both devices, SIMS depth profiling of hydrogen species was performed for both samples. **Figure 2** showed the SIMS depth profiles of OH⁻ and hydrogen concentration in a-IZTO thin films with a passivation stack of SiO_2(200 nm)/SiO_2(300 nm) and SiO_2(200 nm)/Al_2O_3(50 nm)/SiO_2(300 nm). A lower hydrogen concentration including OH⁻ and atomic hydrogen was observed for the Al_2O_3-inserted stack. The 300-nm-thick SiO_2 passivation film was prepared under hydrogen-rich conditions (see the Experimental Section). Therefore, during thermal annealing at 350 °C for 60 min, the diffusion of hydrogen species into the a-IZTO channel layer was suppressed due to the existence of Al_2O_3 films for the Al_2O_3-inserted samples. As mentioned previously, some of the incorporated hydrogen species act as shallow donors. Therefore, the tailing states below the conduction band minimum of a-IZTO semiconductor for the Al_2O_3-inserted field-effect transistors will be less filled because of the lower hydrogen-donated free electrons. Therefore, the higher μ_{SAT} and lower V_{TH} for the control device compared to those of Al_2O_3-inserted devices can be attributed to their larger free electron density as a result of the higher level of hydrogen incorporation because charge carrier transport in the zinc-based oxide semiconductor is governed by a percolation conduction mechanism. The variations in SS values for both devices also need to be considered carefully because of the double-sided character of the hydrogen impurities. The SS values (≈0.10 V decade⁻¹) for the Al_2O_3-inserted a-IZTO TFTs were lower than those (≈0.15 V decade⁻¹) of the control a-IZTO TFTs. The fast bulk trap density (N_{SS}) in the forbidden gap of a-IZTO semiconductor and semiconductor-insulator trap density (D_{it}) can be estimated from the following equation[42]

$$SS = q k_B T (N_{ss} t_{ch} + D_{it}) / [C_i \log(e)], \tag{1}$$

where q is the electron charge, k_B is Boltzmann's constant, T is the absolute temperature, and t_{ch} is the channel layer thickness. The maximum $N_{SS,max}$ ($D_{it,max}$) value in the a-IZTO TFTs was estimated by setting the D_{it} (N_{SS}) value to zero. The $N_{SS,max}$ ($D_{it,max}$) values for the control and Al_2O_3-inserted a-IZTO TFTs were 4.6×10^{16} eV⁻¹ cm⁻³ (2.3×10^{11} eV⁻¹ cm⁻²) and 3.1×10^{16} eV⁻¹ cm⁻³ (1.6×10^{11} eV⁻¹ cm⁻²), respectively. For the benchmarking comparison, these $N_{SS,max}$ values for the a-IZTO

TFTs were lower than those (($1-6$) $\times 10^{17}$ eV⁻¹ cm⁻³) of the IGZO[43] and IZTO[44] TFTs. It should be noted that the lower N_{SS} (D_{it}) values for the a-IZTO TFTs in this study can also come from the different compositions or/and components in the channel layer. The high mobility of the a-IZTO TFTs would be a reflection of the lower N_{SS} distribution in the forbidden band gap of the a-IZTO semiconductor and lower D_{it} value between a-IZTO and SiO_2 film. In addition, the higher N_{SS} value for the control devices compared to the Al_2O_3-inserted devices suggests that the incorporation of hydrogen species can accompany the creation of the defect state as well as the electron doping into a-IZTO channel. For further insight, the density-of-state (DOS) distributions for both devices were extracted using the Meyer–Neldel rule (NMR). Temperature-dependent field effect data were used to calculate the near conduction band. The drain current (I_{DS}) was thermally activated, which can be described by the following equation[45]

$$I_{DS} = I_{DS0} \exp\left(-\frac{E_a}{kT}\right) \tag{2}$$

where I_{DS0} is the prefactor, E_a is the activation energy, K is the Boltzmann constant, and T is the temperature. The E_a of IZTO TFT with different etch-stopper layers is V_{GS}-dependent, and their relationship obeys the MN rule. The MN rule is an intrinsic property of a disordered semiconductor, which has been reported in various organic and inorganic semiconductor materials, including pentacene,[46] a-Si,[47] and a-IGZO.[45] The MN rule is expressed as follows[48]

$$I_{DS0} = I_{DS00} \exp(A \cdot E_a) \tag{3}$$

where A is the MN parameter. Using the MN relation, extraction of the DOS distribution for the a-IZTO TFTs was performed assuming that most induced electron charges are occupied in the localized energy states, and the probability of finding an electron at a certain energy level is determined by the 0 K Fermi statistics, as reported by Chen et al.[45] The total DOS distribution for the sample A and B devices with different etch stopper layers was calculated, as shown in **Figure 3**. The overall DOS distribution for the a-IZTO TFTs with the Al_2O_3 interlayer was smaller than that of the control a-IZTO TFTs over the 0.2–0.3 eV energy range extracted. This agrees with the comparative results for the N_{SS} values calculated from the SS value.

The effects of hydrogen incorporation on the dark PBTS and NBTS instability of the resulting a-IZTO TFTs was investigated. The devices were stressed under the following conditions: V_{GS} at $V_{TH} + 20$ V and $V_{TH} - 20$ V for the PBTS and NBTS, respectively, at room temperature. The V_{DS} was fixed to 5.1 V and the BTS duration was 3600 s. **Figure 4**a,b presents the evolution of the transfer curve as a function of the applied PBTS time for the control and Al_2O_3-inserted device, respectively. For the control device, the parallel V_{TH} shift of 0.41 V to the positive direction after the application of PBTS was observed without an accompanying change in mobility, SS and $I_{ON/OFF}$ ratio. The positive V_{TH} shift for the Al_2O_3-inserted device was reduced drastically to 0.13 V. The superior electrical stability for the Al_2O_3-inserted device was preserved for the NBTS duration: the negative V_{TH} shift for the control and Al_2O_3-inserted device were −6.0 and −1.5 V,
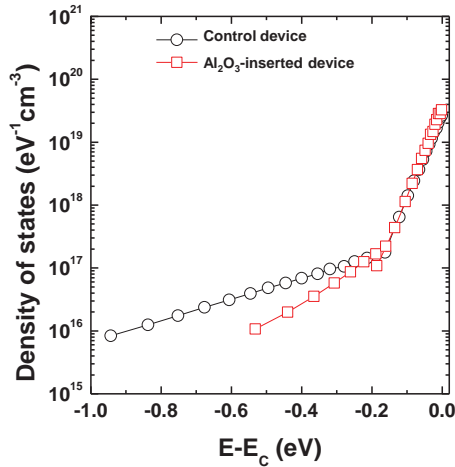
Figure 3. DOS distributions of a) the control and b) Al$_2$O$_3$-inserted a-IZTO TFTs.

respectively, as shown in Figure. 4c,d. The NBIS stability, which is one of the critical figure-of-merits for optoelectronics applications of the a-IZTO semiconductor, was also examined for both devices. The bias thermal stress condition for NBIS instability

was identical to the NBTS except for light irradiation. To amplify the V_{TH} variation of the a-IZTO TFTs during the NBIS applications, the blue LED was used as a light source where the light intensity was 75 µW cm^{-2}. The V_{TH} shift was accelerated by the simultaneous light irradiation on the channel region. **Figure 5**a,b shows the evolution of the transfer characteristics of the control and Al$_2$O$_3$-inserted devices, respectively, as a function of the NBIS time. The control device suffered from a huge negative V_{TH} shift (−8.4 V) during the NBIS duration, whereas the V_{TH} instability for the Al$_2$O$_3$-inserted devices was strongly suppressed (ΔV_{TH} = −3.0 V). It is noted that under only the NBIS condition, the hump near the subthreshold drain current region of the transfer characteristics was observed for both devices (Figure 5) whereas the application of dark PBTS and NBTS into the a-IZTO TFTs caused the parallel displacement of the transfer characteristics without any distortion (Figure 4). The hump occurrence in terms of transfer characteristics depended on the gate bias sweep direction: in the case of reverse gate sweep (V_{GS}: from 15 to −15 V) the hump could not be observed (data not shown). This gate sweep-direction dependent hump occurrence under photon illumination was attributed to either the trapping of the photoinduced hole carriers,[49,50] or the pile-up of ionic defects such as V_O^{2+}[51] and H_i^{+}[52] at the dielectric/channel interface.
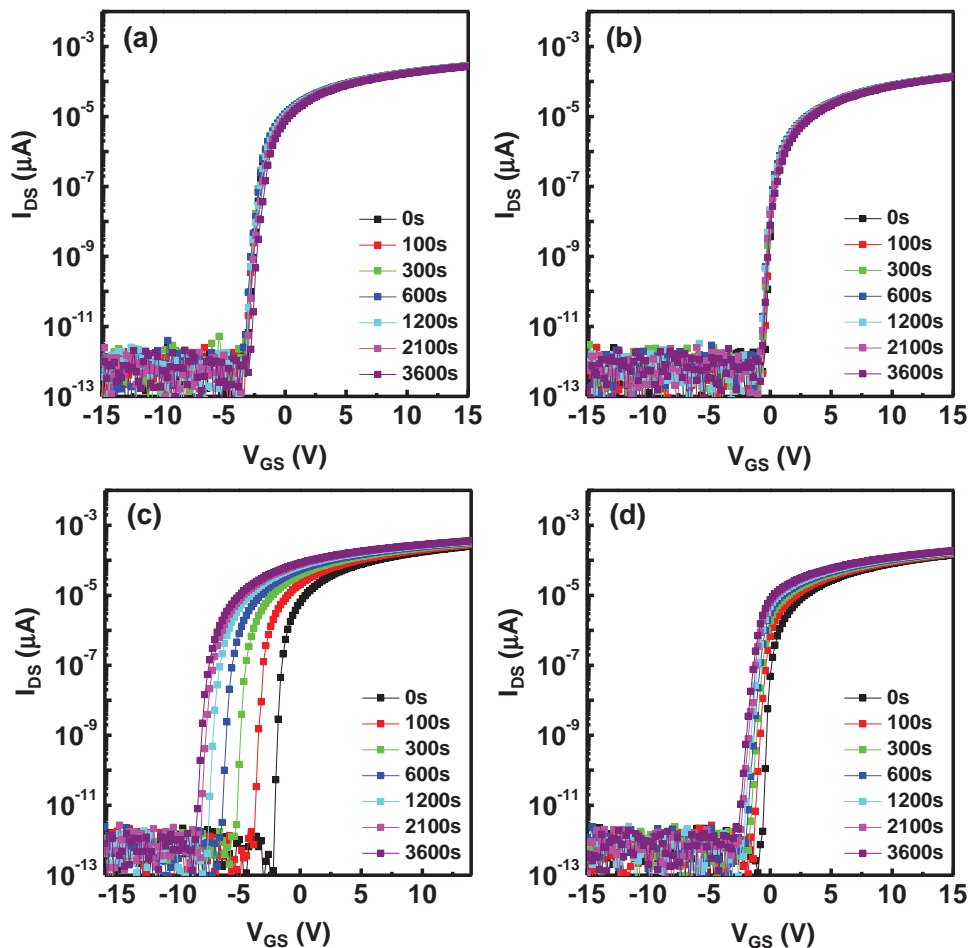

Figure 4. Evolution of the transfer curve as a function of the applied PBTS time for a) the control and b) Al$_2$O$_3$-inserted device. The effect of the NBTS duration on the transfer characteristics for c) the control and d) Al$_2$O$_3$-inserted device.

**ADVANCED
ELECTRONIC
MATERIALS**
www.advelectronicmat.de
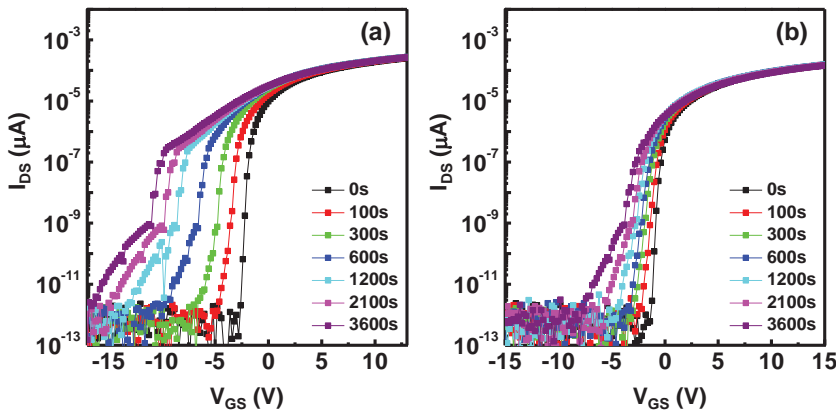
**Materials
Views**
www.MaterialsViews.com

Figure 5. Evolution of the transfer characteristics for a) the control and b) Al$_2$O$_3$-inserted devices, respectively, as a function of the NBIS time. The gate voltage during the transfer curve measurement was sweep from −15 to 15 V (forward sweep).

The activation energy for the NBTS and recovery behavior was examined. **Figure 6** shows the recovery behavior of the C–V characteristics for the control and Al$_2$O$_3$-inserted devices. The C–V curves during the NBTS duration were shifted negatively, which is consistent with the negative V_{TH} shift, as shown in Figure 4c,d. After turning off the NBTS, the C–V curves partially recovered to the original V_{TH} direction. The transition of the charge state in the hydrogen impurities would be strongly related to the activation energy of the NBTS and recovery process. Therefore, the kinetics of the NBTS and recovery process was also investigated. **Figure 7** presents the temperature-dependent V_{TH} variations of both devices as a function of the NBTS time. The data were fitted using a stretched exponential formula[53,54]

$$| \Delta V_{th}(t)| = V_0 \left\{ 1 - \exp\left[-\left(\frac{t}{\tau}\right)^{\beta} \right] \right\}, \qquad (4)$$

where τ is the relaxation time, β is the dispersion parameter of the barrier energy height, and V_0 is $V_{GS} - V_{th0}$ (V_{GS} is the

applied gate bias stress). The relaxation time (τ) was activated thermally according to the following equation[53,54]

$$\tau = v^{-1} \exp\left(\frac{E_\tau}{k_B T} \right), \qquad (5)$$

where E_τ is the activation energy for the process, v is the frequency prefactor for emission over the barrier, T is the absolute temperature, and k_B is the Boltzmann constant. Figure 7b,e presents the variations of ln τ as a function of the reciprocal temperature for the control and Al$_2$O$_3$-inserted devices, respectively. The data were well fitted using Equation (5), suggesting that the devices have a temperature dependence on τ and the NBTS-induced V_{th} shift is a thermally activated process. The $E\tau$ values for the control and Al$_2$O$_3$-inserted devices were calculated from the slope of the straight lines. The $E\tau_{,NBTS}$ values of the control and Al$_2$O$_3$-inserted devices were 0.31 and 0.90 eV under NBTS condition, respectively. Therefore, the inferior NBTS stability of the control IZTO TFTs can be attributed to the lower activation energy of 0.31 eV. This suggests that the a-IZTO materials with a large hydrogen concentration would have a variety of paths to the deep-to-shallow transition in hydrogen impurities. This speculation can be further supported by the smaller β values of the control device, as shown in Figure 7c,f, because the β is a measure of the spread in the $E\tau$ distribution.[55] **Figure 8**a,d shows the temperature-dependent recovery behavior of the V_{TH} value for the control and Al$_2$O$_3$-inserted devices, respectively. To accelerate the recovery process, a positive gate bias stress of V_{TH} + 20 V was applied during the measurements of the transfer curves. From linear fitting between $1/T$ versus ln τ using Equation (5), the $E\tau_{,recovery}$ values extracted for the control and Al$_2$O$_3$-inserted devices were 0.10 and 0.51 eV under PBTS condition, respectively. In addition, the faster recovery for the control device compared to the Al$_2$O$_3$-inserted device, as shown in Figure 6, can also be explained by the smaller $E\tau_{,recovery}$ value of 0.10 eV. The extracted β values for both devices were comparable to those for the NBTS induced transition process.

The difference between the control and Al$_2$O$_3$-inserted devices on the light- and bias-induced instabilities of a-IZTO semiconductors cannot be explained by the well-known mechanisms involving oxygen vacancies. First, the superior PBTS stability for the Al$_2$O$_3$-inserted device can be explained by charge trapping modeling. The amount of the positive V_{TH} shift under the PBTS condition would be proportional to the charge trapping frequency of the accumulated carriers at the defect sites including the gate dielectric and IZTO channel layer. Therefore, the stronger resistance of the Al$_2$O$_3$-inserted device under the PBTS condition appears to
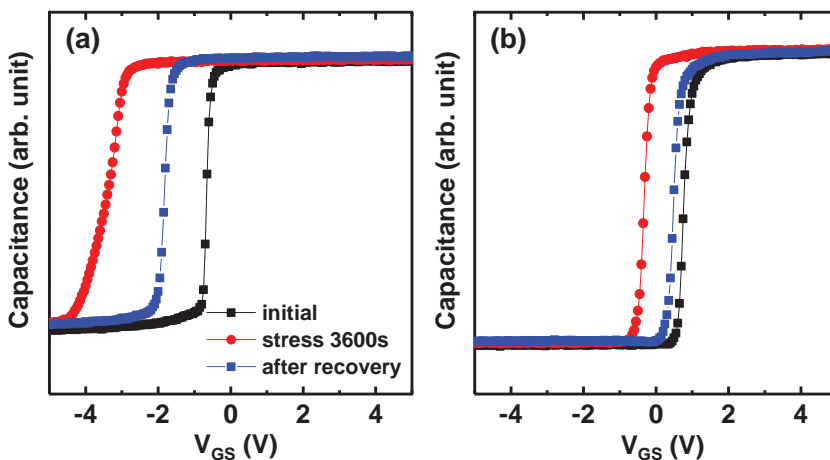

Figure 6. Recovery behavior of the C–V characteristics for a) the control and b) Al$_2$O$_3$-inserted devices, respectively. The C–V curves were shifted to the negative direction during the NBTS duration, which is consistent with the negative V_{TH} shift, as shown in Figure 4c,d. After turning off the NBTS, the C–V curves were recovered partially to the original V_{TH} direction.
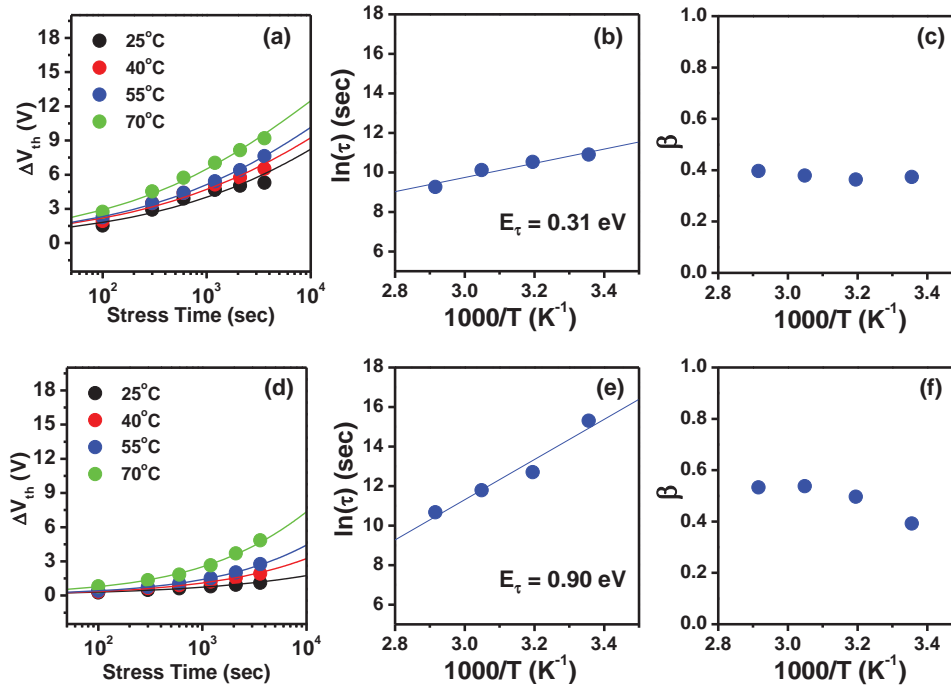
Figure 7. Temperature-dependent V_{TH} variations for a) the control and d) Al_2O_3-inserted devices under the NBTS conditions. Relationship between $1/T$ versus $\ln(\tau)$ for b) the control and e) Al_2O_3-inserted devices. The corresponding dispersion parameter β as a function of the reciprocal temperature for c) the control and f) Al_2O_3-inserted devices.

be due to the lower concentration of tailing states, as shown in Figure 3. This result is well corroborated by the fact that the $N_{SS,max}$ and $D_{it,max}$ values extracted from the SS factor for

the Al_2O_3-inserted device was lower than those for the control device (see Table 1). On the other hand, the origin of the lower tailing states in the Al_2O_3-inserted device is unclear. Moreover,
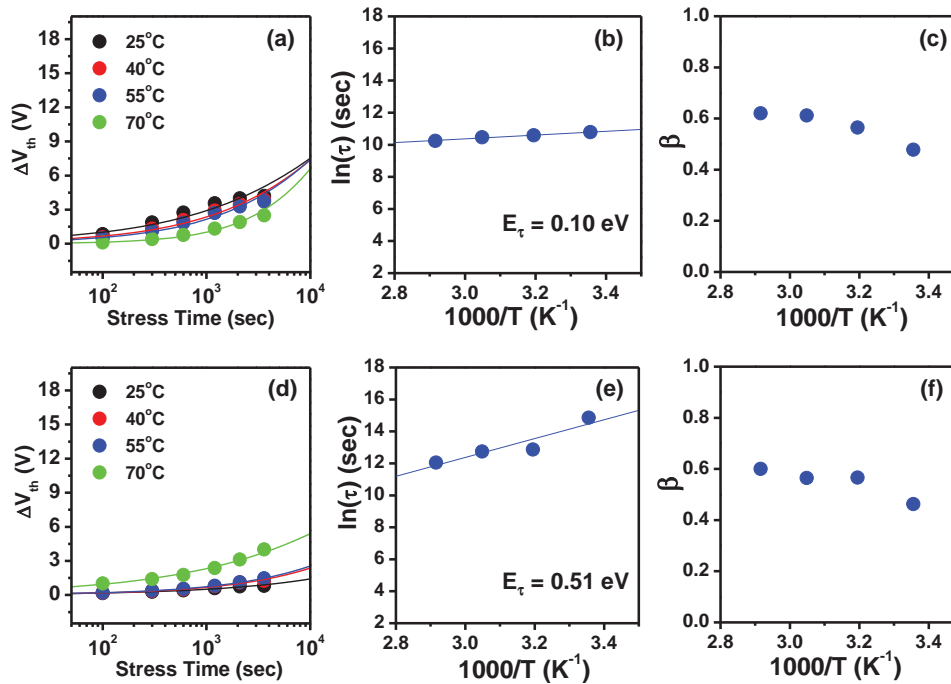

Figure 8. Temperature-dependent V_{TH} variations for a) control and d) Al_2O_3-inserted devices under the PBTS conditions. Relationship between $1/T$ versus $\ln(\tau)$ for b) control and e) Al_2O_3-inserted devices. The corresponding dispersion parameter β as a function of the reciprocal temperature for c) control and f) Al_2O_3-inserted devices.

ADVANCED
ELECTRONIC
MATERIALS
www.advelectronicmat.de

Materials
Views
www.MaterialsViews.com

the reason why the Al_2O_3-inserted device showed better NBTS and NBIS stability is more ambiguous. The NBTS- and NBIS-induced instabilities of the semiconducting oxide TFTs have been understood based mainly on the oxygen vacancy model, which basically suggests an anion (oxygen)-deficiency in the semiconductor layer. The deep oxygen vacancy defect (V_O^0) can be excited into the shallow ionized oxygen vacancy defect (V_O^{2+}) by the application of NBTS or NBIS, leading to free electron carriers in the conduction band and a negative V_{TH} shift of the resulting oxide TFTs. On the other hand, this V_O model cannot explicitly explain the strongly hydrogen content-dependent NBTS and NBIS instabilities for the two samples. Therefore, the fundamental origin of the PBTS, NBTS, and NBIS instability of the a-IZTO TFTs seems to be mainly associated with the electronic structures of the bistable hydrogen impurities.

2.2. Bistable Hydrogen in a-IZTO

In c-ZnO, it is well-known that each type of H impurity at the interstitial and substitutional sites exhibits two different charge states as a bistable center.[27,29,33,34] The shallow H_i^+, which is bonded to an O atom, is stable as a hydroxyl OH^-[27], and acceptor-like deep H_i^-, which is bonded to Zn atoms, is metastable at the hollow site.[33] On the other hand, when H is strongly combined with V_O, shallow H_O^+ is stable in the form of a multicenter bond at the V_O site,[29] and in the negative charge state, the deep H-DX$^-$ is stable compared to the H_O^+ with two additional electrons at conduction band minimum (CBM) (H_O^+ + 2e at CBM).[34] However, since the bistability of the hydrogen impurities in the amorphous phase may be different from those in the crystal, density functional theory (DFT) calculations were performed to determine whether there are deep H centers in a-IZTO or not. We find that similarly to c-ZnO, there can be the acceptor-like deep H-related centers (H_i^- and H-DX$^-$) in amorphous phase, which suggests that the deep H centers can be assigned as a major origin of the carrier-induced instabilities in the oxide TFTs, resulting in a negative shift of V_{TH}.

Figure 9 shows the atomic structure of four kinds of H impurities in a-IZTO, which are similar to those in c-ZnO. In fact, it was difficult to uniquely define the interstitial and substitutional sites in the amorphous phase due to the lack of periodicity, and in principle, all the H impurities become different, indicating that the atomic and electronic structures of the H impurities are slightly or significantly deviated with respect to the crystal phase. In this work, 9, 10, 9, and 6 configurations for each type, H_i^+, H_i^-, H_O^+, and H-DX$^-$, respectively, were sampled individually to statistically analyze
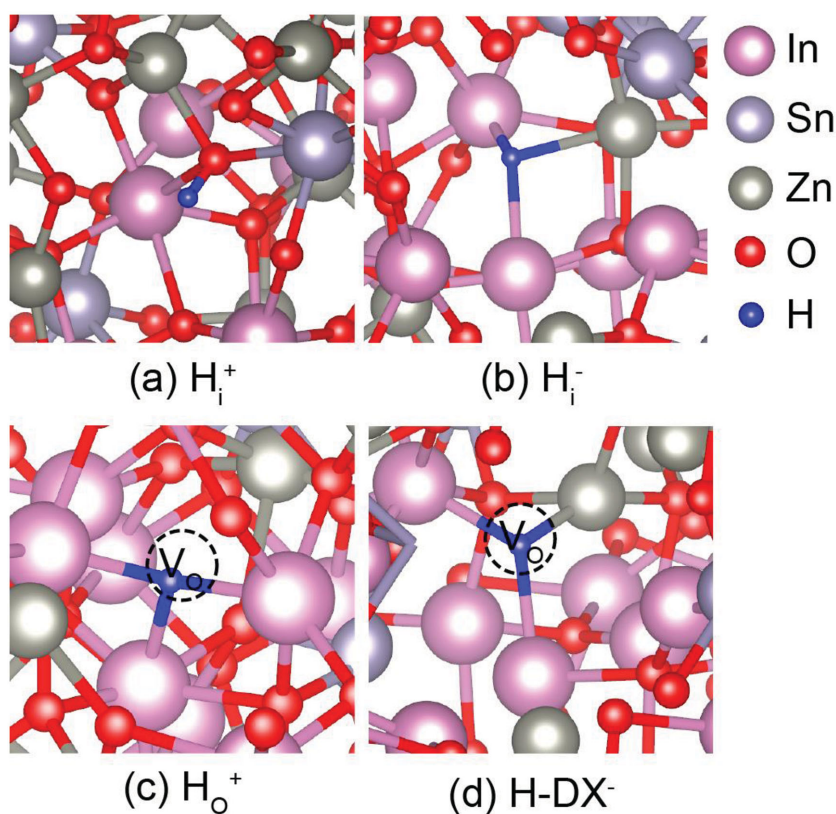

Figure 9. Atomic structures of a) H_i^+, b) H_i^-, c) H_O^+, and d) H-DX$^-$ in a-IZTO material.

the calculated results of H. Nevertheless, the structural and electronic characteristics of H_i^- and H-DX$^-$ in c-ZnO[33,34] were found to be qualitatively conserved in a-IZTO. The summarized results of four H type are shown in **Table 2**. Figure 9a,b shows that H_i^+ and H_i^- for the interstitial case are bonded with O and cations atoms, respectively, because of the delicate balance of the Coulomb and quantum mechanical interactions between H and the host atoms (In^{3+}, Sn^{4+}, Zn^{2+}, and O^{2-}). For the substitutional case, while H_O^+ has Zn surrounding the location of the host O atom, as shown in Figure 9c, the H in H-DX is largely displaced from on-site H_O site into an interstitial H_i one (leaving a V_O) through large lattice relaxation (LLR), resulting in a complex defect of $V_O^0 + H_i^-$, as shown in Figure 9d. Interestingly, as our expectation, H_i^- and H-DX$^-$ have deep impurity levels, as shown in **Figure 10**a,b, whereas all the H_i^+ and H_O^+ are shallow, which plays the role of donating an electron into the host. Moreover, because a-IZTO is an amorphous phase,

Table 2. Summarized results including structural and electronic characteristics on four types of hydrogen impurities (i.e., H_i^+, H_i^-, H_O^+, and H-DX$^-$ ($V_O^0 + H_i^-$)).

	Defect type	Charge state	Type of neighboring atoms (M = metal)	Electronic impurity levels (eV) (E_C = CBM)
H_i^+	Interstitial	+1	O–H	$> E_C$
H_i^-	Interstitial	−1	M–H	about E_C-2.45
H_O^+	Substitutional	+1	M–H	$> E_C$
H-DX$^-$	Substitutional	−1	M–H	about E_C-1.58

www.MaterialsViews.com

ADVANCED
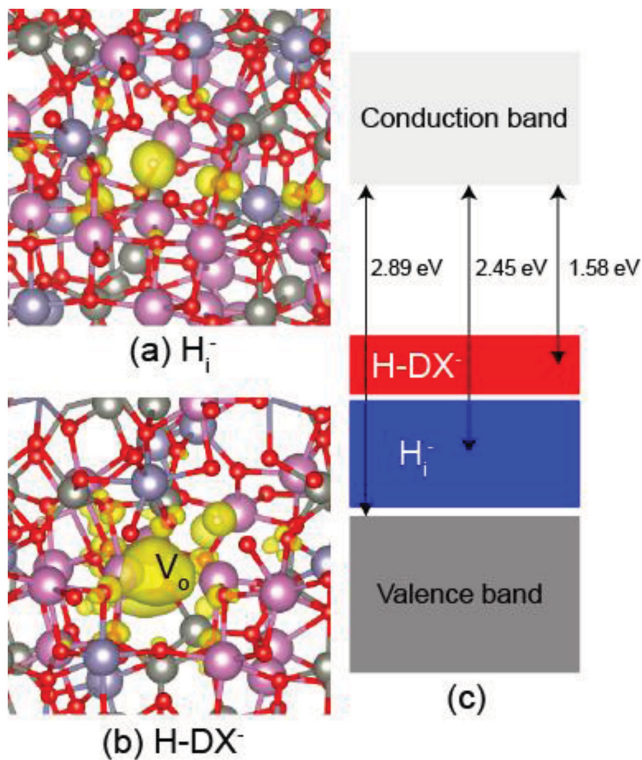ELECTRONIC
MATERIALS
www.advelectronicmat.de

FULL PAPER

Figure 10. Partial charge densities of a) H_i^- and b) H-DX$^-$ electronic states. c) The schematic diagram of the energy distributions of the H levels.

the deep levels of H_i^- and H-DX$^-$ are located broadly above the VBM, as shown in Figure 10c. The impurity levels of H_i^- are found to be distributed more widely and deeper compared to those of H-DX$^-$. The average minimum excitation energies that are required for the direct transition of electrons from the impurity level to CBM were calculated separately to be 2.45 and 1.58 eV for H_i^- and H-DX$^-$, respectively. Therefore, H-DX$^-$ is active compared to H_i^- on the visible light (low energy) illumination or the thermal excitation.

To assess the thermal stability of each H impurity in a-IZTO, the formation energy (E_f) was calculated using the following equation

$$E_f = E_t^i - E_t^p - \sum_i \Delta n_i \mu_i + q E_F, \qquad (6)$$

where E_t^i is the total energy of a supercell containing the impurity (defect) with a q-charge state, E_t^p is the total energy of a perfect supercell, and Δn_i and μ_i are the change in the number of atoms in the supercell and the chemical potential, respectively. For the charged supercell calculations, the spurious monopole electrostatic interaction was corrected within the Makov and Payne scheme.[56] Here, it was considered to be the O- and H-rich condition, in which μ_O and μ_H are given by a half of the total energy of O_2 and H_2 molecules, respectively. The Fermi level (E_F) is an electronic chemical potential, where valence band maximum (VBM) is aligned to zero. Therefore, the position of E_F corresponds to CBM when E_F equals the band

gap. Because of the underestimation of the calculated band gap in the conventional DFT calculations, the band gap correction scheme was used to estimate E_f by applying the quasiparticle (QP) shifts of both the band edges, which are adjusted by the weight-average on the composition rate of a-IZTO (based on the QP shifts of the crystal In_2O_3, SnO_2, and ZnO in ref. [57] to be the experimental band gap. The QP-shifted values for VBM and CBM, considering the difference between the experimental (3.19 eV) and theoretical (1.30 eV) optical band gaps, were calculated to be −0.48 and 1.41 eV, respectively. The relatively large QP shift of CBM in a-IZTO is consistent with that of amorphous $InGaZnO_4$.[58]

Figure 11 shows the calculated formation energies, E_fs, of the four types of H impurities. Because the E_fs of each type in amorphous phase are distributed widely due to a deficiency of periodicity, they were averaged out on the tested configurations of H_i^+, H_i^-, H_O^+, and H-DX$^-$, respectively, to show the deviation width for each type. The averaged thermal transition level, $\varepsilon(+/-)_{av}$, from H_i^+ (H_O^+) to H_i^- (H-DX$^-$) was 2.79 (2.96) eV above the VBM. Therefore, regardless of the existence of V_O (O-chemical potential), in most regions of E_F, H_i^+ and H_O^+ are more stable than H_i^- and H-DX$^-$, indicating that H can be one of the sources for n-type conductivity of a-IZTO. On the other
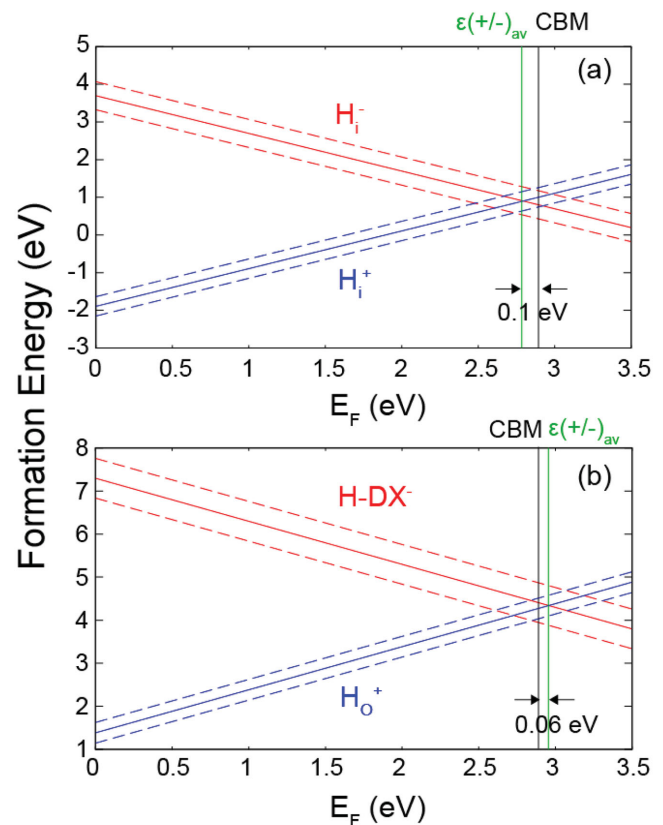

Figure 11. Formation energies of a) H_i^+ (blue lines), H_i^- (red lines), b) H_O^+ (blue lines), and H-DX$^-$ (red lines) with respect to the Fermi level (E_F) assuming H-rich and O-rich conditions. The averaged thermal transition levels ($\varepsilon(+/-)_{av}$s) for H_i and H_O are noted by the vertical (green) lines, respectively. The solid and dashed lines indicate the average value and the deviation of the formation energies, respectively. 0 of E_F corresponds to VBM.
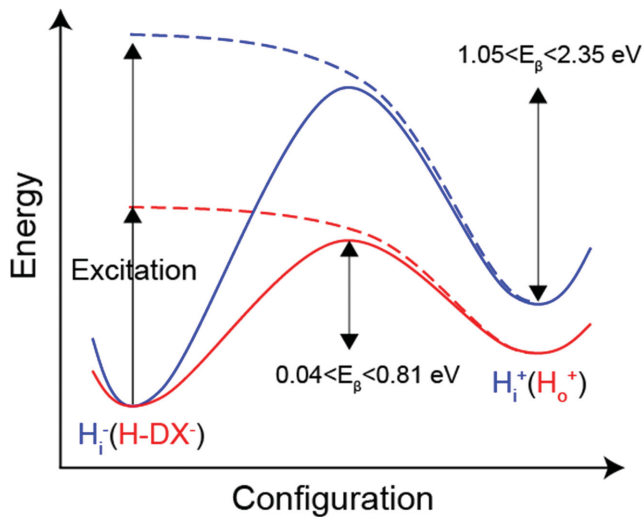
ADVANCED
ELECTRONIC
MATERIALS
www.advelectronicmat.de

Materials
Views
www.MaterialsViews.com

Figure 12. Schematic configuration-energy diagrams for the transition of the charge states between H_i^- (H-DX$^-$) and H_i^+ (H$_O^+$). The solid red and blue lines denote the transitions from H_i^- to H_i^+ and H-DX$^-$ to H$_O^+$, respectively, in the negative charge state. The dashed red and blue lines indicate the energy curves for the structural transitions of H_i and H_O, respectively, when the electrons are excited to the conduction band in the positive charge state.
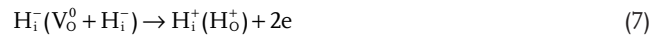
hand, H_i^- and H-DX$^-$ were energetically comparable to H_i^+ and H_O^+ when E_F is close to CBM. Thus, this indicates that the H_i^+, H_O^+, H_i^-, and H-DX$^-$ states can coexist in the n-type semiconducting a-IZTO, depending on the growth and annealing conditions. Furthermore, remarkably, the $\varepsilon(+/-)_{av}$ of H_i is found to be slightly lower than that of H_O. In the semiconducting a-IZTO with the carrier concentration of the 10^{17} cm^{-3} order, which was located approximately (below) at CBM, the concentration of the deep H-DX$^-$ should be changed more sensitively than that of the deep H_i^-, because the difference in the E_fs between H_O^+ and H-DX$^-$ for H_O is smaller than that for H_i at E_F.

The total energy profiles of the structural transformation between the H_i^- (H-DX$^-$) and H_i^+ (H$_O^+$) in the charge states of (+) and (−) were calculated. **Figure 12** shows a schematic configuration-energy diagram for the transition of the charge states between H_i^- (H-DX$^-$) and H_i^+ (H$_O^+$). When the electrons at the deep H level are excited, the H_i^- (H-DX$^-$) structure is relaxed spontaneously to H_i^+ (H$_O^+$) structure approximately with an energy barrier of zero ($E_\alpha \approx 0.0$ eV). The energy barriers (E_βs) for the structural recovery from the H_i^+ and H_O^+ to H_i^- and H-DX$^-$ were estimated to be large within $1.05 < E_\beta < 2.05$ eV and small within $0.04 < E_\beta < 0.81$ eV, respectively. The recovery of some structural deformation to the original states requires a significant thermal energy barrier. In particular, the energetic barrier for the transition from H_i^+ to H_i^- exhibited a relatively large value compared to that from H_O^+ to H-DX$^-$, because a strong O–H bond needs to be broken.

2.3. Microscopic Mechanism of Hydrogen on Electrical Instabilities in a-IZTO

The bistable hydrogen impurities can explain the microscopic origin of the negative or positive shifts of the V_{TH}

with their fast or slow recovery processes under the NBTS or light stress conditions. As mentioned above, the H_i^+, H_O^+, H_i^-, and H-DX$^-$ (=V$_O^0$ + H_i^-) states can coexist in the a-IZTO sample, depending on the growth condition. Therefore, when external stresses, such as light illumination or negative electric field, can cause electron excitation from deep H_i^- and H-DX$^-$ states to CBM, the large structural relaxation near the H site is instantly induced without an energy barrier (due to $E_\alpha \approx 0.0$ eV) as follows:

$$H_i^- (V_O^0 + H_i^-) \rightarrow H_i^+ (H_O^+) + 2e \tag{7}$$

Based on the H-transition mechanism, the H-donated electrons induce transient or persistent enhancement of the electron concentration in a-IZTO, resulting in the device instabilities (negative V_{th} shift). For the recovery process, when H_i^+ (H$_O^+$) captures two mobile electrons at CBM, structural recovery from the H_i^+ (H$_O^+$) to H_i^- (H-DX$^-$) can be occurred as follows

$$H_i^+ (H_O^+) + 2e \rightarrow H_i^- (V_O^0 + H_i^-) \tag{8}$$

The NBTS-induced transition and PBTS-induced recovery energy barriers (see schematic total energy profiles in Figure 12) through the thermal process are distributed diversely for the H impurity, which indicates that the transition and recovery can occur with fast or slow times, depending on the H type and its local configuration.

First, the superior results for the Al$_2$O$_3$-inserted device in terms of the PBTS instabilities to the control device can be explained based on the hydrogen model. Because the application of PBTS on a-IZTO TFTs raises the E_F toward the CBM, the H_i^- (H-DX$^-$) charge state is favored compared to the H_i^+ (H$_O^+$) charge state. Therefore, the prolonged PBTS duration on the a-IZTO TFTs causes conversion from the shallow H defect states (H_i^+ and H_O^+) to the acceptor-like deep defect states (H_i^- and H-DX$^-$). This E_F-induced conversion process would consume the free electron carriers in the channel region, leading to a positive V_{TH} shift in the resulting devices. Therefore, the superior PBTS stability of the Al$_2$O$_3$-inserted device was attributed to the lower existence (concentration) of shallow H defects states, which is corroborated with the results of Figure 4a,b.

Second, the NBTS and NBIS instabilities for both devices can also be understandable in the frame of the hydrogen model. When NBS is applied to the a-IZTO TFTs, the quasi-E_F in the channel region near the gate dielectric/semiconductor interface moves the VBM downward due to the carrier depletion effect. The lowering of quasi-E_F in the a-IZTO layer facilitates the transformation from the H_i^- (or H-DX$^-$) charge state to the H_i^+ (H$_O^+$) charge state, which accompanies the capture of a hole carrier or emitting of an electron carrier (see Figure 11). These deep-to-shallow transitions of hydrogen impurities cause electron doping in the conduction band, leading to a negative V_{TH} shift of the resulting devices. Therefore, the bistabilities of hydrogen impurities are the origin for the inferior instability of the control device under the NBTS and NBIS condition.

Third, the large difference between the activation barriers of the control device and those of Al$_2$O$_3$-inserted device

during NBTS, as shown in Figures 7 and 8, respectively, can be explained qualitatively by the bistable H_i^- and H-DX$^-$ states. This is based on the differently calculated properties of the thermal transition level ($\varepsilon(+/-)_{av}$), the H level within band gap, and the recovery energy barrier ($E\beta$ in Figure 12) for both H types. The measured free electron concentration in the control device was higher than that in Al_2O_3-inserted device. In the control device with a high electron concentration (corresponding to a high value in $\approx 10^{17}$ cm^{-3}), E_F lies at approximately 0.02 eV below the CBM (much closed to CBM), and in the Al_2O_3-inserted device with a low electron concentration (corresponding to a low value in $\approx 10^{17}$ cm^{-3}), the E_F lies at approximately 0.08 eV below the CBM. Therefore, although both H_i^- and H-DX$^-$ in the control device are possibly available, the formation energy of H-DX$^-$ in the Al_2O_3-inserted device is metastable with respect to H_O^+, suggesting that the concentration of H-DX$^-$ is reduced drastically compared to the shallow H_O^+ state (see Figure 11). For this reason, by default, both H_i^- and H-DX$^-$ in the control device with a large H concentration coexist, whereas H_i^- exists mainly in the Al_2O_3-inserted device with a small H concentration.

For the transition energy barrier in NBTS to excite the electrons at the deep level without light illumination on both the control and Al_2O_3-inserted devices (Figure 7), instability occurs by thermal excitation from the deep state into the E_F, and during the NBTS process, this can more easily occur due to the upward-bending of the electronic structures at the a-IZTO interface. It is noteworthy that the thermal excitation energy for H_i^- is largely required, compared to that of H-DX$^-$ because the impurity level of H_i^- (located at 2.45 eV below CBM) is deeper by 0.85 eV than that of H-DX$^-$ (located at 1.58 eV below CBM), as shown in Figure 10 and Table 2. In the case of the control device having both H_i^- with large barriers and H-DX$^-$ with small barriers, the transition energy barrier would be more active by the low-barrier H-DX$^-$ because the transition of chemical state dominantly occurs along with a low energy pathway. On the other hand, the Al_2O_3-inserted device can be dominated by the transition of large-barrier H_i^- because H-DX$^-$ with small barriers is barely formed in the Al_2O_3-inserted device. This indicates that the transition energy barriers in the control device and Al_2O_3-inserted device are predominantly determined by H-DX$^-$ and H_i^-, respectively, which results in the higher transition energy barrier ($E_{\tau,NBTS}$) of the Al_2O_3-inserted device compared to the control device. However, it is noted that it is difficult to quantitatively compare experimental results with theoretical ones because experimental measurements are performed under the conditions different from theoretical calculations (i.e., negative electric field and corresponding quasi-E_F). Nevertheless, the significant difference (≈ 0.85 eV) in the averaged thermal excitation energy of H-DX$^-$ and H_i^-:0.85 eV is qualitatively consistent with the large difference (≈ 0.59 eV) in the activation energy barrier ($E_{\tau,NBTS}$) for the control and Al_2O_3-inserted device, which were experimentally determined to be 0.31 and 0.90 eV, respectively.

The recovery energy barrier qualitatively corresponds to the E_β values in the $H_i^+(H_O^+) \rightarrow H_i^-(V_O^0 + H_i^-)$ transitions, as shown in the configurational energy diagram of Figure 12.

The E_β values for each type, interstitial H_i and substitutional H_O, were calculated to be largely separated. The reason for the different recovery barriers of both devices can also be attributed to the aforementioned rationale. In case of the control device with the coexistence of both H_O and H_i types, the recovery barrier ($E_{\tau,recovery}$) is mostly determined by H-DX$^-$ with low energy barriers. Conversely, H_i with large energy barriers for the Al_2O_3-inserted device dictates the recovery process, which causes its $E_{\tau,recovery}$ value to be larger than that for the control device. The present recovery process was measured under an applied positive bias (Figure 8) to raise the E_F near the interface. Compared to the E_β values calculated without consideration of an externally applied positive bias (see Figure 12), the experimentally determined recovery barrier should decrease with increasing E_F, suggesting that the experimental recovery barrier of 0.51 eV can be understood qualitatively by the positive-bias-induced reduction of the calculated E_β values.

In addition, bistable hydrogen impurities are at least an origin for the positive and negative V_{TH} shift of the oxide TFTs in a variety of samples. Depending on the cation composition, the cation/anion ratio in the prepared semiconducting oxide film and the integration processing condition, the major source of the instabilities can be considered differently, e.g., V_O, peroxide (O_2^{2-}) and O-interstitial. It is also noted that the gate field-assisted generation and migration of ionic defects such as V_O^{2+}, Zn_i^{2+}, and H_i^+ etc., can also partially contribute to the observed BTS-induced instabilities of the a-IZTO TFTs,[52,53,59] which was not fully considered in this study. In particular, these defect generation and migration during BTS duration can be accelerated under light illumination and elevated temperature because the incident photon and thermal energy into a-IZTO film are likely to facilitate the creation and/or migration of the specific point defects. The combined experimental and theoretical study of BTS and light-induced defect creation and migration in metal oxide semiconductor is being conducted, which will be reported elsewhere.

3. Conclusion

The hydrogen-rich control a-IZTO TFTs exhibited a high μ_{SAT} of 48.0 cm^2 Vs^{-1}, low SS of 0.15 V decade^{-1}, V_{TH} of 0.4 V, and $I_{ON/OFF}$ ratio of 10^9. On the other hand, the μ_{SAT} and V_{TH} for the hydrogen-poor Al_2O_3-inserted a-IZTO TFTs were reduced to 20.5 cm^2 Vs^{-1} and increased to 1.4 V, which can be attributed to the lower n-type doping concentration of shallow hydrogen defects. The Al_2O_3-inserted a-IZTO TFTs showed much better stability than the control device under PBTS, NBTS, and NBIS conditions, indicating that the hydrogen-related defects have an adverse effect on the bias and photo-bias stabilities of the devices. The activation energies for NBTS and recovery behavior were extracted from the analysis based on the stretched exponential formula. The $E_{\tau,NBTS}$ and $E_{\tau,recovery}$ values for the control device were 0.31 and 0.10 eV, respectively whereas the significant larger $E_{\tau,NBTS}$ (0.9 eV) and $E_{\tau,recovery}$ (0.51 eV) values were obtained for the Al_2O_3-inserted device. The H_i and H_O in a-IZTO material were calculated to be bistable centers with an electronic

deep-to-shallow transition through large lattice relaxation. In case of control device, the H_i^- with large barrier and H-DX$^-$ with small barriers coexist due to the higher free electron concentration and thus elevated E_F level closing to CBM. Therefore, the low-barrier H-DX$^-$ dictates the transition and recovery process, which resulted in the smaller $E_{\tau,NBTS}$ and $E_{\tau,recovery}$ values for the control device energy leading to the inferior gate bias stability. Conversely, the Al_2O_3-inserted device is dominated by the transition of large-barrier H_i^- because H-DX$^-$ with small barriers are barely formed in the hydrogen-poor a-IZTO material, which is responsible for its higher $E_{\tau,NBTS}$ and $E_{\tau,recovery}$ values and thus, the superior gate-bias stability. These finding can provide a comprehensive single framework to understand the PBTS, NBTS, and NBIS instability of a-IZTO TFTs based on the simultaneous consideration of well-known V_O (or O_2^{2-}, O_i) and hydrogen impurities. It is concluded that delicate controllability of hydrogen and balancing the anion/cation ratio are a key factor to achieve the high performance and stability of the metal oxide transistor.

4. Experimental Section

Device Fabrication and Electrical Characterization: Figure 1 presents a schematic cross-section of an integrated a-IZTO TFT. The DC sputter-derived molybdenum film was patterned through the photolithography and wet etching process, which was used as the gate electrode on a glass substrate. The 300-nm-thick SiO_2 film as a gate insulator (GI) was deposited by plasma-enhanced chemical vapor deposition (PECVD). For the active channel layer, a-IZTO film was prepared by DC sputtering at room temperature with the target composition of In_2O_3:ZnO:SnO_2 = 40:40:20 at% and patterned by the photolithography and wet etch processes using diluted HF. A 200-nm-thick SiO_2 film as an ESL was then coated by PECVD (control device). To control the level of hydrogen doping in the a-IZTO semiconductor, an additional 50-nm-thick Al_2O_3 film with an excellent barrier property against the hydrogen permeation was deposited on the ESL/a-IZTO/GI/Mo/glass substrate by rf sputtering, which is referred to as a-IZTO TFTs with a Al_2O_3 interlayer. After defining the contact hole for the source/drain (S/D) electrode using photolithography and dry etching, the Mo film as the S/D electrode was deposited by DC sputtering and patterned by the standard wet etching process. Finally, the 300-nm-thick SiO_2 was deposited as the passivation layers by PECVD, where the high silane flow rate of 150 sccm was used to provide high hydrogen content in the SiO_2 passivation layer. It is noted that this high SiH_4 flow rate for the PECVD-derived SiO_2 film corresponds to the standard condition. After fabricating the a-IZTO TFTs, these devices were annealed at 350 °C for 60 min in a furnace. During thermal annealing, the hydrogen was expected to diffuse into the a-IZTO semiconductor through the ESL from the SiO_2 passivation layer. The channel width (W) and length (L) for the a-IZTO TFTs investigated were 54 and 10 μm, and the gate-to-S/D overlap length (L_{ov}) was fixed to 3 μm. The initial electrical characterics including the transfer (I_{DS}–V_{GS}) and capacitance–voltage (C–V) characteristics were measured at room temperature using an Agilent 4156 semiconductor parameter analyzer and HP 4294 LCR meter under a dark ambient conditions. The SIMS depth profiles using the Bi^+ primary ion beams with energies of 25 keV–1 pA were obtained to compare the relative level of hydrogen incorporation in the IZTO semiconductor film for both devices.

Theoretical Calculation: The DFT calculations of a-IZTO were performed using the Vienna ab inito simulation package (VASP) with the projector-augmented wave (PAW) pseudopotential, and the PBE functional was used to calculate the exchange-correlation energy. First-principles molecular dynamics (MD) simulations were carried out to obtain the amorphous structure. To generate the final amorphous structure more efficiently, the atoms in a cubic supercell were first distributed randomly with the constraints on the bond lengths between M–M, M–O, and O–O, which allows shortening of the melting time. A supercell containing 10 formula units of $In_2SnZn_2O_7$ was constructed and heated to 3000 K for 10 ps and cooled rapidly to 300 K at a rate of −300 K ps^{-1}. The final amorphous structure was obtained by full relaxation of the cell volume and atomic positions.

For the structural relaxation and electronic structure calculation, on-site Coulomb energy (U) was added for the localized d electrons of metals, which partially corrects the band gap underestimation of the conventional DFT calculation in this material by reducing the repulsion interaction between O-p and M-d. The U values of In-d, Sn-d, and Zn-d were 5.0, 3.5, and 7.5 eV, respectively. The kinetic energy cutoff of the plane wave basis was 500 eV and the single k-point of (0.25, 0.25, 0.25) was used. The k-point convergence was tested, and the total energy deviation was within 10 meV per atom.

[1] K. Nomura, H. Ohta, A. Takagi, T. Kamiya, H. Hirano, H. Hosono, *Nature* **2004**, *432*, 488.

[2] E. Fortunato, P. Barquinha, R. Martins, *Adv. Mater.* **2012**, *24*, 2945.

[3] H. Chen, Y. Cao, J. Zhang, C. Zhou, *Nat. Commun.* **2014**, *5*, 4097.

[4] T. Kamiya, K. Nomura, H. Hosono, *Sci. Technol. Adv. Mater.* **2010**, *11*, 044305.

[5] J. K. Jeong, *Semicond. Sci. Technol.* **2011**, *26*, 034008.

[6] J. S. Park, W.-J. Maeng, H.-S. Kim, J.-S. Park, *Thin Solid Films* **2012**, *520*, 1679.

[7] Y.-H. Kim, J.-S. Heo, T.-H. Kim, S. Park, M.-H. Yoon, J. Kim, M. S. Oh, G.-R. Yi, Y.-Y. Noh, S. K. Park, *Nature* **2012**, *489*, 128.

[8] H. Yabuta, M. Sano, K. Abe, T. Aiba, T. Den, H. Kumomi, K. Nomura, T. Kamiya, H. Hosono, *Appl. Phys. Lett.* **2006**, *89*, 112123.

[9] H. Hosono, *J. Non-Cryst. Solids* **2006**, *352*, 851.

[10] J.-S. Park, K. S. Kim, Y.-G. Park, Y.-G. Mo, H. D. Kim, J. K. Jeong, *Adv. Mater.* **2009**, *21*, 329.

[11] C.-J. Kim, S. Kim, Y. Park, J. H. Kim, S. T. Shin, U-I. Chung, *Appl. Phys. Lett.* **2009**, *95*, 252103.

[12] J. K. Jeong, *J. Mater. Res.* **2013**, *28*, 2071.

[13] K. Ghaffazadeh, A. Nathan, J. Roberson, S. Kim, S. Jeong, C. Kim, U-I. Chung, J. H. Lee, *Appl. Phys. Lett.* **2010**, *97*, 113504.

[14] K. Ghaffazadeh, A. Nathan, J. Roberson, S. Kim, S. Jeong, C. Kim, U-I. Chung, J. H. Lee, *Appl. Phys. Lett.* **2010**, *97*, 143506.

[15] M. D. H. Chowdhury, P. Migliorato, J. Jang, *Appl. Phys. Lett.* **2010**, *97*, 173506.

[16] H. Oh, S-M. Yoon, M. K. Ryu, C-S. Hwang, S. Yang, S.-H. K. Park, *Appl. Phys. Lett.* **2010**, *97*, 183502.

[17] B. S. Yang, S. Park, S. Oh, Y. J. Kim, J. K. Jeong, C. S. Hwang, H. J. Kim, *J. Mater. Chem.* **2012**, *22*, 10994.

[18] K. H. Ji, J.-I. Kim, H. Y. Jung, S. Y. Park, R. Choi, U. K. Kim, C. S. Hwang, D. Lee, H. Hwang, J. K. Jeong, *Appl. Phys. Lett.* **2011**, *98*, 103509.

www.MaterialsViews.com

ADVANCED
ELECTRONIC
MATERIALS
www.advelectronicmat.de

FULL PAPER

[19] Y.-M. Kim, K.-S. Jeong, H.-J. Yun, S.-D. Yang, S.-Y. Lee, Y.-C. Kim, J. K. Jeong, H.-D. Lee, G.-W. Lee, *Appl. Phys. Lett.* **2013**, *102*, 173502.

[20] K. Ide, Y. Kikuchi, K. Nomura, M. Kimura, T. Kamiya, H. Hosono, *Appl. Phys. Lett.* **2011**, *99*, 093507.

[21] J. Robertson, Y. Guo, *Appl. Phys. Lett.* **2014**, *104*, 162102.

[22] D. J. Chadi, K. J. Chang, *Phys. Rev. Lett.* **1988**, *61*, 873.

[23] S. Lany, A. Zunger, *Phys. Rev. B* **2005**, *72*, 035215.

[24] A. Janotti, C. G. Van de Walle, *Appl. Phys. Lett.* **2005**, *87*, 122102.

[25] B. Ryu, H.-K. Noh, E.-A. Choi, K. J. Chang, *Appl. Phys. Lett.* **2010**, *97*, 022108.

[26] H.-H. Nahm, Y.-S. Kim, D. H. Kim, *Phys. Status Solidi B* **2012**, *249*, 1277.

[27] C. G. Van de Walle, *Phys. Rev. Lett.* **2000**, *85*, 1012.

[28] C. G. Van de Walle, J. Neugebauer, *Nature* **2003**, *423*, 626.

[29] A. Janotti, C. G. Van de Walle, *Nat. Mater.* **2007**, *6*, 44.

[30] T. Kamiya, K. Nomura, H. Hosono, *Phys. Status Solidi A* **2010**, *207*, 1698.

[31] S. W. Tsao, T. C. Chang, S. Y. Huang, M. C. Chen, S. C. Chen, C. T. Tsai, Y. J. Kuo, T. C. Chen, W. C. Wu, *Solid State Electron.* **2010**, *54*, 1497.

[32] H.-K. Noh, J.-S. Park, K. J. Chang, *J. Appl. Phys.* **2013**, *113*, 063712.

[33] M.-H. Du, K. Biswas, *Phys. Rev. Lett.* **2011**, *106*, 115502.

[34] H.-H. Nahm, C. H. Park, Y.-S. Kim, *Sci. Rep.* **2014**, *4*, 4124.

[35] K. Nomura, T. Kamiya, H. Hosono, *ECS J. Solid State Sci. Technol.* **2013**, *2*, P5.

[36] H.-K. Noh, K. J. Chang, B. Ryu, W.-J. Lee, *Phys. Rev. B* **2011**, *84*, 115205.

[37] S. Y. Park, J. H. Song, C.-K. Lee, B. G. Son, C.-K. Lee, H. J. Kim, R. Choi, Y. J. Choi, U. K. Kim, C. S. Hwang, H. J. Kim, J. K. Jeong, *IEEE Electron Device Lett.* **2013**, *34*, 894.

[38] J. H. Song, K. S. Kim, Y. G. Mo, R. Choi, J. K. Jeong, *IEEE Electron Device Lett.* **2014**, *35*, 853.

[39] L. Wang, M. Yoon, G. Lu, Y. Yang, A. Facchetti, T. J. Marks, *Nat. Mater.* **2006**, *5*, 893.

[40] H. W. Zan, W. W. Tsai, C. H. Chen, C. C. Tsai, *Adv. Mater.* **2011**, *23*, 4237.

[41] X. Liu, C. Wang, B. Cai, X. Xiao, S. Guo, Z. Fan, J. Li, X. Duan, L. Liao, *Nano Lett.* **2012**, *12*, 3596.

[42] D. W. Greve, *Field Effect Devices and Applications: Devices for Portable, Low-Power, and Imaging Systems*, Prentice Hall, Upper Saddle River, NJ **1998**, p. 379.

[43] J. K. Jeong, J. H. Jeong, H. W. Yang, J.-S. Park, Y. G. Mo, H. D. Kim, *Appl. Phys. Lett.* **2007**, *91*, 113505.

[44] M. K. Ryu, S. Yang, S.-H. K. Park, C.-S. Hwang, J. K. Jeong, *Appl. Phys. Lett.* **2009**, *95*, 072104.

[45] C. Chen, K. Abe, H. Kumomi, J. Kanichi, *IEEE Trans. Electron Devices* **2009**, *56*, 1177.

[46] E. J. Meijer, N. Matters, P. T. Herwig, D. M. de Leeuw, T. M. Klapwijk, *Appl. Phys. Lett.* **2000**, *76*, 3433.

[47] R. E. I. Schropp, J. Snijder, J. F. Verwey, *J. Appl. Phys.* **1986**, *60*, 643.

[48] W. Meyer, H. Neldel, *Z. Technol. Phys.* **1937**, *18*, 588.

[49] D. W. Kwon, J. H. Kim, J. S. Chang, S. W. Kim, W. Kim, J. C. Park, C. J. Kim, B.-G. Park, *IEEE Trans. Electron. Devices* **2011**, *58*, 1127.

[50] Y. S. Rim, W. Jeong, B. D. Ahn, H. J. Kim, *Appl. Phys. Lett.* **2013**, *102*, 143503.

[51] Y. J. Chung, J. H. Kim, U. K. Kim, M. Ryu, S. Y. Lee, C. S. Hwang, *Electrochem. Solid-State Lett.* **2011**, *14*, H300.

[52] H. J. Kim, S. Y. Park, H. Y. Jung, B. G. Son, C.-K. Lee, C.-K. Lee, J. H. Jeong, Y. G. Mo, K. S. Son, M. K. Ryu, S. Lee, J. K. Jeong, *J. Phys. D: Appl. Phys.* **2013**, *46*, 055104.

[53] M. D. H. Chowdhury, P. Migliorato, J. Jang, *Appl. Phys. Lett.* **2011**, *98*, 153511.

[54] S. G. J. Mathijssen, M. Cölle, H. Gomes, E. C. P. Smits, B. Boer, I. McCulloch, P. A. Bobbert, D. M. Leeuw, D M, *Adv. Mater.* **2007**, *19*, 2785.

[55] J. Luo, A. U. Adler, T. O. Mason, D. B. Buchholz, R. P. H. Chang, M. Grayson, *J. Appl. Phys.* **2013**, *113*, 153709.

[56] G. Makov, M. C. Payne, *Phys. Rev. B* **1995**, *51*, 4014.

[57] Y. Kang, G. Kang, H.-H. Nahm, S.-H. Cho, Y. S. Park, S. Han, *Phys. Rev. B* **2014**, *89*, 165130.

[58] Y. Kang, H. Song, H.-H. Nahm, S. H. Jeon, Y. Cho, S. Han, *APL Mater.* **2014**, *2*, 032108.

[59] Y.-M. Kim, K.-S. Jeong, H.-J. Yun, S.-D. Yang, S.-Y. Lee, Y.-C. Kim, J.-K. Jeong, H.-D. Lee, G.-W. Lee, *Appl. Phys. Lett.* **2013**, *102*, 173502.